Acta Oceanol. Sin., 2024, Vol. 43, No. 0, P. 1–13
https://doi.org/10.1007/s13131-024-2326-7
http://www.aosocean.com
E-mail: ocean2@hyxb.org.cn

The sudden ocean warming and its potential influences on early–frozen landfast ice in Prydz Bay, East Antarctica

Haihan Hu[1, 2], Jiechen Zhao[3, 4*], Jingkai Ma[5], Igor Bashmachnikov[6, 7], Natalia Gnatiuk[6, 7], Bo Xu[8], Fengming Hui[1, 2*]

[1] School of Geospatial Engineering and Science, Sun Yat-sen University, and Southern Marine Science and Engineering Guangdong Laboratory (Zhuhai), Zhuhai 519082, China

[2] Key Laboratory of Comprehensive Observation of Polar Environment (Sun Yat-sen University), Ministry of Education, Zhuhai 519082, China

[3] Qingdao Innovation and Development Base (Centre) of Harbin Engineering University, Qingdao, 266500, China

[4] Key Laboratory for Polar Acoustics and Application of Ministry of Education (Harbin Engineering University), Harbin 150001, China

[5] Key Laboratory of Research on Marine Hazards Forecasting, National Marine Environmental Forecasting Centre, Beijing 100081, China

[6] Nansen International Environmental and Remote Sensing Centre, St. Petersburg 199034, Russia

[7] Saint Petersburg State University, St. Petersburg, 199034, Russia

[8] Antarctic Great Wall Ecology National Observation and Research Station, Polar Research Institute of China

Received 20 December 2023; accepted 20 March 2024

Abstract

The ocean conditions beneath the ice cover play a key role in understanding the sea ice mass balance in the Polar Regions. An integrated high-frequency ice–ocean observation system, including Acoustic Doppler Velocimeter (ADV), Conductivity Temperature and Depth (CTD) Sensor, and Sea Ice Mass Balance Array (SIMBA), was deployed in the landfast ice region close to the Chinese Zhongshan Station in Antarctica. A sudden ocean warming of 0.14℃ ($p < 0.01$) was observed beneath early–frozen landfast ice, from (–1.60 ± 0.03)℃ during April 16–19 to (–1.46 ± 0.07)℃ during April 20–23, which is the only significant warming event in the nearly 8-month records. The sudden ocean warming brought a double rise in oceanic heat flux, from (21.7 ± 11.1) W/m^2 during April 16–19 to (44.8 ± 21.3) W/m^2 during April 20–23, which shifted the original growth phase at the ice bottom, leading to a 2 cm melting, as shown from SIMBA and borehole observations. Simultaneously, the slowdown of ice bottom freezing decreased salt rejection, and the daily trend of observed ocean salinity changed from +0.02/d during April 16–19, to +0.003/d during April 20–23. The potential reasons are increased air temperature due to the transit cyclones and the weakened vertical ocean mixing due to the tide phase transformation from semi-diurnal to diurnal. The high-frequency observations within the ice–ocean boundary layer enhance the comprehensive investigation of the ocean's influence on ice evolution at a daily scale.

Key words: sudden ocean warming, oceanic heat flux, landfast ice, Zhongshan Station, *in-situ* observation

Citation: Hu Haihan, Zhao Jiechen, Ma Jingkai, Bashmachnikov Igor, Gnatiuk Natalia, Xu Bo, Hui Fengming. 2024. The sudden ocean warming and its potential influences on early–frozen landfast ice in Prydz Bay, East Antarctica. Acta Oceanologica Sinica, 43(0): 1–13, doi: 10.1007/s13131-024-2326-7

1 Introduction

Sea ice is a fundamentally important component of the Antarctic climate system (Parkinson and Cavalieri, 2012; Stammerjohn et al., 2012; Singh et al., 2021). Its seasonal growth and retreat affect almost every aspect of the Antarctic system, from atmospheric stability and ocean dynamics to ice sheet mass balance and biological productivity (Maykut and Untersteiner, 1971; McMinn et al., 2000; Heil, 2006; Massom et al., 2009, 2010; Miles et al., 2017; Moreau et al., 2020). Correspondingly, the seasonal change of sea ice is also affected by the seasonal thermodynamic ice-ocean feedbacks (Himmich et al., 2023; Purich and Doddridge, 2023). Decadal hindcasts showed that the Southern Ocean subsurface warming has persisted and gradually destabilised the ocean, becoming one of the influential factors in the dramatic changes observed in Antarctic sea ice (Meehl et al., 2019; Zhang et al., 2022). Oceanic heat flux is an essential parameter in determining the thermodynamical thickness of sea ice (Maykut and Untersteiner, 1971; Ebert et al., 1995; Zhao et al., 2017a; Guo et al., 2019). Oceanic heat flux is related to the heat storage and turbulent mixing in the boundary layer (McPhee, 1992). Sea ice growth and melt are determined by the heat balance between the oceanic heat flux and the conductive heat transfer through the overlying ice cover (Maykut, 1986). Accurately quantifying the changes in heat flux caused by ocean warming is essential for understanding the process of sea ice growth.

Landfast ice near Zhongshan Station, East Antarctica, usually

Foundation item: The National Natural Science Foundation of China under contract Nos 42276251, 42211530033, and 41876212; the Taishan Scholars Program.

*Corresponding author, E-mail: zhaojiechen@hrbeu.edu.cn; huifm@mail.sysu.edu.cn

attached to the coastline, shelf edge, and grounded icebergs. In contrast with pack ice, landfast ice has a longer annual duration and is generally thicker, and its growth is mainly influenced by thermodynamic processes (Heil et al., 1996; Heil, 2006; Lei et al., 2010; Zhao et al., 2017a, 2019; Li et al., 2023). The ice growth or melt rate at the ice–ocean interface is determined by the heat flux balance between that transmitted through the ice layer and that supplied to the ice bottom by the ocean (Lytle et al., 2000; Lei et al., 2022). Previous studies in the coastal regions of Prydz Bay suggest that oceanic heat flux has a seasonal cycle with the maximum flux in early–frozen stages (Allison, 1981; Heil et al., 1996; Lei et al., 2010; Yang et al., 2016; Zhao et al., 2019; Hu et al., 2023). These studies have mainly focused on seasonal variations in oceanic heat flux. At the same time, because it is difficult to observe the oceanic heat flux directly, most studies used the heat balance equation based on the sea ice bottom to calculate the oceanic heat flux (residual method).

The ice growth rate is relatively high in the early-frozen stages due to cold air forcing. The rapid rejection of brine by sea ice makes the thermohaline environment of sea water beneath sea ice change rapidly, which makes the change of oceanic heat flux more intense. To further explore the variations of ocean temperature, salinity, velocity and oceanic heat flux on the growth of landfast ice, a set of high-resolution ice–ocean observation equipment was deployed on the landfast ice about 1 km away from Zhongshan Station, including an acoustic Doppler velocimeter (ADV), conductivity–temperature–depth (CTD) sensors, and a sea ice mass balance array (SIMBA).

Previous researchers have studied oceanic heat flux under landfast ice near the Zhongshan Station, based on the residual method. Li et al. (2023) analysed observations from IMB buoys near Zhongshan Station from 2013 to 2018 and found that during the early–frozen stages, the rapid growth rate and salt rejection process resulted in relatively large oceanic heat flux in June (about 22 W/m^2). Lei et al. (2010) obtained an oceanic heat flux of approximately 20 W/m^2 in April 2006 based on field measurements and Yang et al. (2016) reported 25 W/m^2 based on model estimates. Zhao et al. (2019) found that the F_w remained at 20–40 W/m^2 during the initial ice growth period in 2012. Compared to the residual method, the direct high frequency measurements of ocean parameters in the mixed layer can provide more accurate estimates of oceanic heat flux by the bulk parameterisation method, as the previous studies conducted in the Arctic and Antarctic (McPhee, 1992; Maykut and McPhee, 1995; McPhee et al., 1996, 2008; Sirevaag, 2009; Sirevaag and Fer, 2009; Kirillov et al., 2015; Peterson et al., 2017; Lei et al., 2022; Hu et al., 2023).

Based on the high-frequency observations during 2021 near Zhongshan Station, Hu et al. (2023) revealed the seasonal variations of oceanic heat flux beneath the landfast ice and further determined that the high-frequency time series of oceanic heat flux exhibited larger perturbations than the residual methods, and more important, higher peaks were found during sudden ocean warming event. To further investigate the atmosphere-snow-ice-ocean interactions during those unusual sudden warming, this study chose the significant event that occurred in April as an example and focused on the synoptic scale, a period of 7-day, to analyse the sudden ocean warming during the early–frozen season.

Therefore, this study is an extent to Hu et al. (2023), and the data used focuses on the time series in April. By analysing the variations in ocean temperature, salinity, and current, along with their impact on oceanic heat flux, this study also tries to discuss the potential influence of the tide and cyclones on the sea ice evolution on a synoptic scale.

The details of observations and methods are presented in Section 2. The observations were deeply analysed and fully described in Section 3. The relationship between air-ice-ocean is discussed in Sections 4 and 5. The conclusions are presented in Section 6. This paper will help better understand the oceanic effects on the diurnal scale of landfast ice growth in Prydz Bay, Antarctica.

2 Data and methods

2.1 *Field observations*

Chinese Zhongshan Station is located in Prydz Bay, East Antarctica (69°22′S, 76°22′E) (Fig. 1a). It was established in February 1989 and operated year-round from then on. The extent of land-

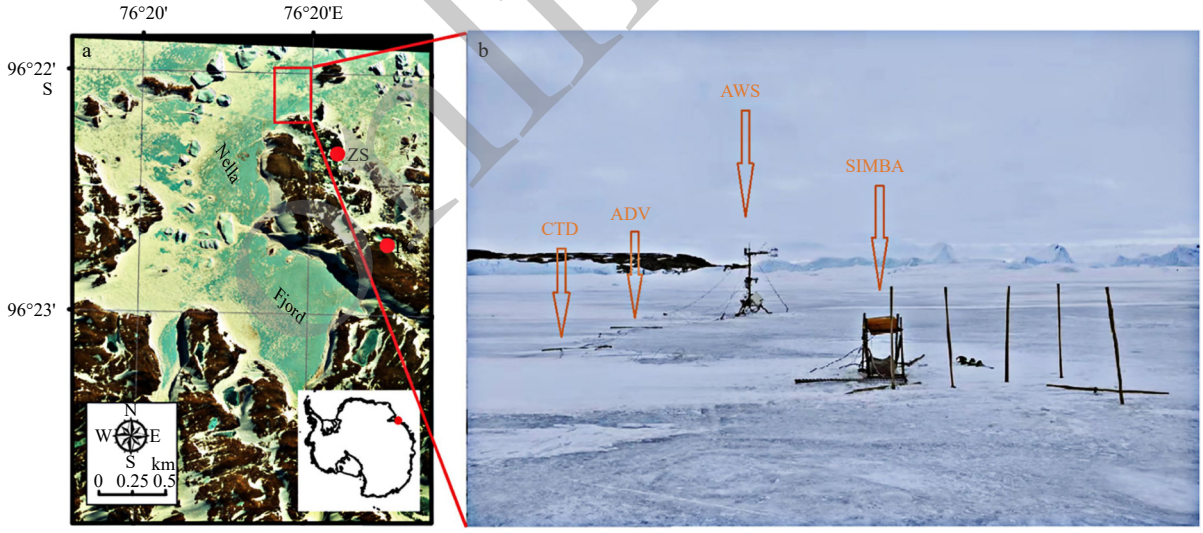

Fig. 1. Satellite image of the observation site in Nella Fjord near Zhongshan Station, modified from the WorldView–2 multi-bands image taken on October 20 2012 (https://worldview.earthdata.nasa.gov) (a) and Photo of the observation site shot in December 2021 (b). ZS, XXX; PG, XXX; CTD, Conductivity Temperature and Depth Sensor; ADV, Acoustic Doppler Velocimeter; AWS, XXX; SIMBA, Sea Ice Mass Balance Array. CTD, ADV, and SIMBA distances were about 5–15 m.

fast ice may reach 60–100 km north of Zhongshan Station in the cold season and break up due to the mechanical forcing in the austral summer (Li et al., 2020; Zhao et al., 2020). In 2021, an integrated high-frequency ice–ocean observation system was established by the wintering team of Zhongshan Station from April on the coastal landfast ice about 1 km off Zhongshan Station (Fig. 1b). A cable-type CTD (model: ALEC ACTD-DF) was deployed 2 m beneath the ice surface, which records ocean temperature, conductivity (salinity) and depth. The measurement frequency was set to 30 s for the salinity (conductivity) and temperature sensors, with accuracy of ±0.02 mS/cm (±0.03) for conductivity (salinity) and ±0.02℃ for temperature. An Acoustic Doppler Velocimeter (model: SonTek Argonaut-ADV) was deployed 5 m below the ice surface, with a 3-D ocean velocity sensor and one temperature sensor. The frequency for velocity and temperature observations was 40 s, and the velocity sensor accuracy was ±0.001 m/s. A Sea Ice Mass Balance Array (model: SRSL SIMBA) was deployed north of the CTD. The SIMBA contained 240 temperature sensors mounted on the thermistor string with 2 cm intervals to measure the vertical temperature profile across the air-snow-ice-ocean column every 6 h. The SIMBA temperature sensors had a resolution of ±0.062 5°C. As per the instrument deployment, the study numbered the temperature sensors from the lowest to the highest. According to the instrument records, the sensor labelled 180 was positioned on the surface of the sea ice, suggesting that around 1.2 m of the temperature chain remained in the atmosphere above the ice surface. Also, the sea ice thickness was under 0.5 m throughout the week, signifying that roughly 3 m of the temperature chain lay beneath the bottom of the sea ice. Snow depth and ice thickness were measured manually around the observation site by the wintering team members.

A data quality control was applied to the original time series to eliminate the anomalous values. All the time series were integrated into 2-min intervals for the convenience of the inter-comparisons. The study used observational data from April 16 to 23, during which all instruments were operational. The analysis was confined to a brief period due to technical issues with the equipment.

2.2 *Reanalysis products*

In this study, the reanalysis data was utilized to investigate the potential impact of polar cyclones on local atmosphere and ice cover conditions. The European Centre for Medium-Range Weather Forecasts (ECMWF) provides a European Reanalysis dataset (ERA). ERA5 is the fifth generation ECMWF reanalysis for the global climate and weather for the past eight decades. Reanalysis combines model data with observations from worldwide into a globally complete and consistent dataset using the laws of physics (Hersbach et al., 2020). It provides hourly estimates for atmospheric and horizontal grid resolutions of 0.25° × 0.25°. The ERA5 dataset is freely accessible at https://cds.climate.copernicus.eu. This study obtained hourly mean sea level pressure over Prydz Bay in Antarctica from April 16 to 24 in the ERA5 reanalysis dataset.

2.3 *Methods of ocean-to-ice heat flux calculation*

Ocean-to-ice heat flux, also known as oceanic heat flux underneath the ice, can be parameterised by many formulas according to the available parameters we observed in the ocean-ice-atmosphere boundary layer (McPhee, 1979, 1992; McPhee and Untersteiner, 1982; McPhee et al., 2008). This study adopted two parameterisations, residual method and bulk parameterisation, as described below.

2.3.1 *Residual method*

The residual method used here to calculate oceanic heat flux is a modified version of the classical Stefan Law. It estimates oceanic heat fluxes by analysing ice vertical temperature profiles and measuring ice bottom growth or ablation. This method has been widely used in previous studies (McPhee and Untersteiner, 1982; Lytle et al., 2000; Perovich and Elder, 2002; Purdie et al., 2006; Lei et al., 2010; Zhao et al., 2019). At the ice bottom, the heat flux balance could be expressed as follows:

$$F_{\mathrm{w}} = F_{\mathrm{c}} + F_{\mathrm{l}} + F_{\mathrm{s}}, \tag{1}$$

where F_{w} and F_{c} are the oceanic and conductive heat flux, respectively. F_{l} is the latent heat flux caused by the freezing or melting of the sea ice, and F_{s} is the specific heat flux generated by the change in ice temperature. In Eq. (1), the signs of melting, heating, and upward heat flow are positive; otherwise, they are negative.

The heat flux terms and freezing point T_{f} can be further expressed as follows (Semtner, 1976; Millero, 1978; Lei et al., 2014):

$$F_{\mathrm{c}} = k_{\mathrm{i}} \frac{T_0 - T_{\mathrm{f}}}{h}, \tag{2}$$

$$F_{\mathrm{l}} = -\rho_{\mathrm{i}} L_{\mathrm{i}} \frac{\mathrm{d}H}{\mathrm{d}t}, \tag{3}$$

$$F_{\mathrm{s}} = \rho_{\mathrm{i}} c_{\mathrm{i}} h \frac{\mathrm{d}T}{\mathrm{d}t}, \tag{4}$$

$$-T_{\mathrm{f}} = 0.0575 S_{\mathrm{w}} - 1.710523 \times 10^{-3} S_{\mathrm{w}}^{3/2} + 2.154996 \times 10^{-4} S_{\mathrm{w}}^{2}, \tag{5}$$

where k_{i} is the ice thermal conductivity; T_0 is the ice temperature in the reference layer (details are provided in Section 4.1); h is the ice thickness of the reference layer and was set to 0.2 m, according to McPhee and Untersteiner (1982); ρ_{i} is the landfast ice density; L_{i} and c_{i} are the latent and specific heat capacity of the sea ice; H is ice thickness and $\mathrm{d}H/\mathrm{d}t$ is the ice growth rate; $\mathrm{d}T/\mathrm{d}t$ is the temporal gradient of ice temperature (Untersteiner, 1961; Millero, 1978; McPhee and Untersteiner, 1982; Lei et al., 2010, 2014; Zhao et al., 2022). T_0 was measured by the SIMBA buoy, and S_{w} was ocean salinity measured by CTD in this study. The ice thickness (H) were estimated from SIMBA buoy, according to the method of Zhao et al. (2017b).

2.3.2 *Bulk parameterisation*

The bulk parameterisation of oceanic heat flux relies on the direct measurements of the high-frequency current velocity, temperature, and salinity in the ice-ocean boundary layer beneath the ice cover, which is called the bulk parameterisation method (McPhee, 1992; McPhee et al., 2008). F_{w} could be calculated by the following formula (Guo et al., 2015):

$$F_{\mathrm{w}} = \rho_{\mathrm{w}} c_{\mathrm{w}} \langle w' T' \rangle, \tag{6}$$

where ρ_{w} is the ocean density, c_w is the specific heat capacity of the ocean; $\langle w' T' \rangle$ is the turbulent heat flux.

The ocean density (ρ_{w}) is a function of temperature and salinity. Millero and Poisson (1981) proposed an internationally recognised atmospheric equation for the state of the ocean, which is calculated as follows:

$$\rho_w - \rho_0 = AS_w + BS_w^{3/2} + CS_w^2, \quad (7)$$

where, ρ_0 is the absolute densities, and could be calculated using the value for pure water from (Bigg, 1967):

$$\rho_0\ (\mathrm{kg \cdot m^{-3}}) = 999.842594 + 6.793952 \times 10^{-2} T_w - 9.095290 \times 10^{-3} T_w^2 + 1.001685 \times 10^{-4} T_w^3 - 1.120083 \times 10^{-6} T_w^4 + 6.536332 \times 10^{-9} T_w^5. \quad (8)$$

The coefficients A, B, and C could be calculated as below (Millero and Poisson, 1981):

$$A = 8.24493 \times 10^{-1} - 4.0899 \times 10^{-3} T_w + 7.6438 \times 10^{-5} T_w^2 - 8.2467 \times 10^{-7} T_w^3 + 5.3875 \times 10^{-9} T_w^4, \quad (9)$$

$$B = -5.72466 \times 10^{-3} + 1.0227 \times 10^{-4} T_w - 1.6546 \times 10^{-6} T_w^2, \quad (10)$$

$$C = 4.8314 \times 10^{-4}, \quad (11)$$

where S_w and T_w are ocean salinity and temperature, which CTD measured in this study.

The heat transferred from the ocean to the ice depends on both the turbulent stress at the ice–ocean interface (characterised by frictional velocity u_0^* as the square root of the kinetic stress at the interface) and the effective ocean heat content in the turbulent boundary layer, which is roughly proportional to the height of the ocean temperature above freezing point (McPhee, 1992; McPhee et al., 1999; Kirillov et al., 2015). The turbulent heat flux could be parameterised as:

$$\langle w'T' \rangle = c_H u_0^* \Delta T, \quad (12)$$

where c_H is the Stanton number of heat exchange efficiency; ΔT is usually expressed as the difference between the ocean temperature and the freezing point; and u_0^* is the friction velocity at the interface. The exchange coefficient c_H are constant of 0.005 7 (McPhee, 2002). Therefore, Eq. (6) could be expressed as:

$$F_w = \rho_w c_w c_H u_0^* \Delta T. \quad (13)$$

Based on the methods mentioned in the previous study (McPhee, 1979), the friction velocity u_0^* can be expressed as follow:

$$u_0^* = \sqrt{0.0104^* V^{1.78}}, \quad (14)$$

where $\boldsymbol{V}$ is the absolute velocity relative to the motionless landfast ice, which the ADV observed in this study.

3 Ocean features beneath ice during the sudden warming

3.1 *Sudden warming and increased variability of ocean temperature*

The CTD sensor measured ocean temperature and salinity at 2 m beneath the landfast ice surface. During April 16–23, 2021, the upper ocean layer beneath the ice showed an average temperature of (–1.53 ± 0.08)℃, while the ice temperature at the bottom (approximately 0.1 m above the ice bottom) was (–3.12 ± 0.71)℃. Consequently, heat flux transfer from warm water to ice is due to the temperature difference. A jump in ocean temperature was observed on April 20 (Fig. 2). During April 16–19, the mean ocean temperature was (–1.60 ± 0.03)℃ and the maximum was –1.50℃, while the mean significantly increased to (–1.46 ± 0.07)℃ and the maximum rose to –1.29℃ during April 20–23. The sudden increase was significant, with a confidence level of 99%. The mean standard deviation also showed a significant increase from 0.03℃ to 0.07℃. The largest daily deviation was 0.35℃ on April 21, while only 0.12℃ on April 18.

The warmer ocean may allow more heat flux into the ice bottom, balancing the conductive heat flux and inhibiting sea ice growth. This is confirmed by the observed basal melt of 2 cm by SIMBA, as shown in Section 4.2.

3.2 *Gradual increase of ocean salinity and density*

Ocean salinity remained at 33.35 ± 0.03; the most significant daily deviation was 0.13 on April 16, and the smallest was 0.06 on April 19 (Fig. 3). The mean increasing trend was significant (0.02/d) during April 16 to 19 and then small (0.003/d) during April 20 to 23, which might be related to the slowdown of the ice bottom freezing due to the increase of the ocean temperature, which paused the salt rejection to the ocean.

The ocean density exhibited a similar increasing trend during April 16–23 (Fig. 4). The mean ocean density was (1 026.84 ± 0.02) kg/m^3. The mean increasing trend was 0.01 (kg · m^{-3})/d during April 16–19, while largely reduced to 0.003 (kg · m^{-3})/d during April 20–23. The daily deviation of ocean density varied between 0.05 kg/m^3 and 0.11 kg/m^3.

3.3 *Periodic oscillation of ocean current*

The 3-D velocity of ocean current at 5 m beneath the ice surface was obtained by ADV. Figure 5 shows the velocity in the meridional (U-component), zonal (V-component), vertical (W-component), and horizontal speed (vector sum of U-component and V-component). During April 16–23, ocean currents showed periodic oscillation, with a mean horizontal speed of about 3 cm/s and a maximum of up to 10 cm/s. The 2-min mean time series showed that 98% of the U-component and 95% of the V-component varied within ±5 cm/s, and 98% of the W-component varied within ±1 cm/s.

To further analyse the time series, the EMD decomposition was used to retain the high-frequency component (Huang et al., 1998). Then, the periodogram method was used to detect the periodicity of the time series (Welch, 1967). The power spectrum analysis shows that a significant half-day period appeared in the U-component, V-component and horizontal speed but not in the W-component. The domain oscillation periods of ocean currents transferred from half-day during April 16–19 to quarter-day, half-day, and one day during April 20–23 (Fig.6).

The rose diagram of the 2-min mean horizontal speed is shown in Fig.7. The domain direction (34%) was southeast (120°–150°), and 70% of the velocity was within 2–8 cm/s. In the study area, the southeast direction means onshore current, which brings warm water in the deep sea to the shallow shore, leading to a jump in ocean temperature.

4 Influence of ocean-to-ice heat flux on ice evolution

4.1 *Sudden increase of ocean-to-ice heat flux*

To further investigate the effect of sudden warming events on the growth of landfast ice, ocean-to-ice heat flux was calculated using two methods, the residual method and bulk method, similar to Hu et al. (2023).

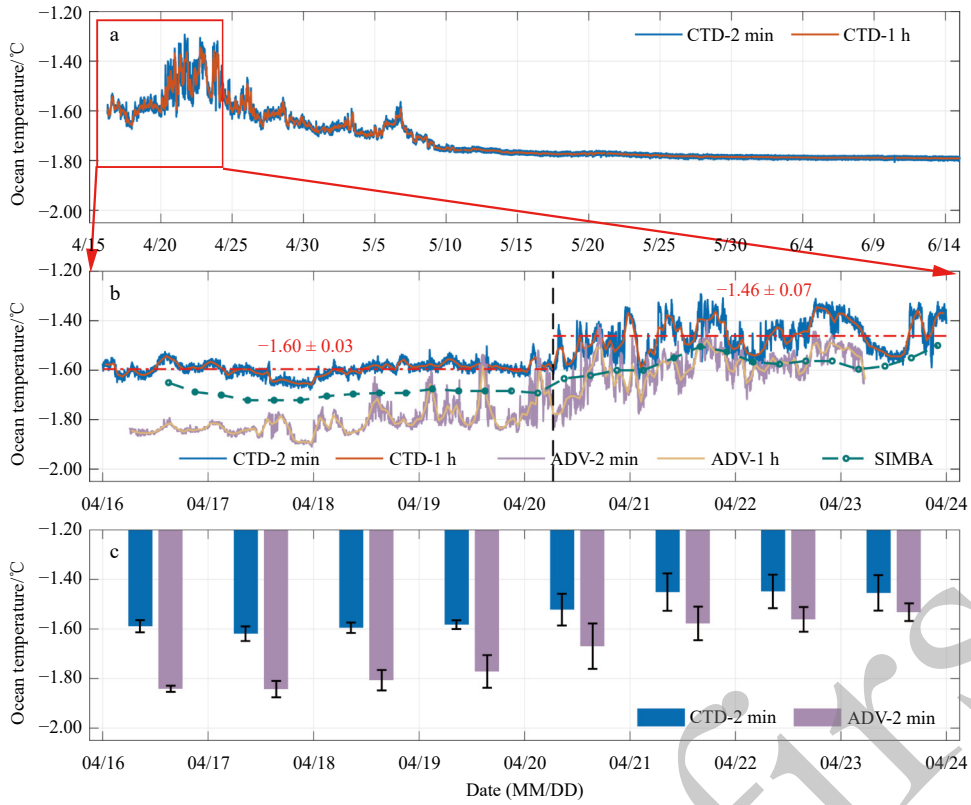

Fig. 2. The ocean temperature observed by CTD at 2 m beneath the landfast ice surface from April 16 to June 15 (a), ocean temperatures were observed by CTD, ADV and SIMBA from April 16 to 23 at different locations below the landfast ice surface (b), and the mean ocean temperature and standard deviation (error bars) of each day (c). In a and b, the green line is the temperature obtained by the SIMBA temperature chain, the average data from five temperature sensors down the ice bottom; the blue line is the ocean temperature data measured by CTD at 2 m beneath the landfast ice surface, and the purple line is the ocean temperature data measured by ADV at 5 m beneath the landfast ice surface; the horizontal coordinate of the black dotted line is the abrupt point calculated using the Mann-Kendall test (06:00 on April 20), and the red dotted line is the mean ocean temperature obtained by CTD during two periods.

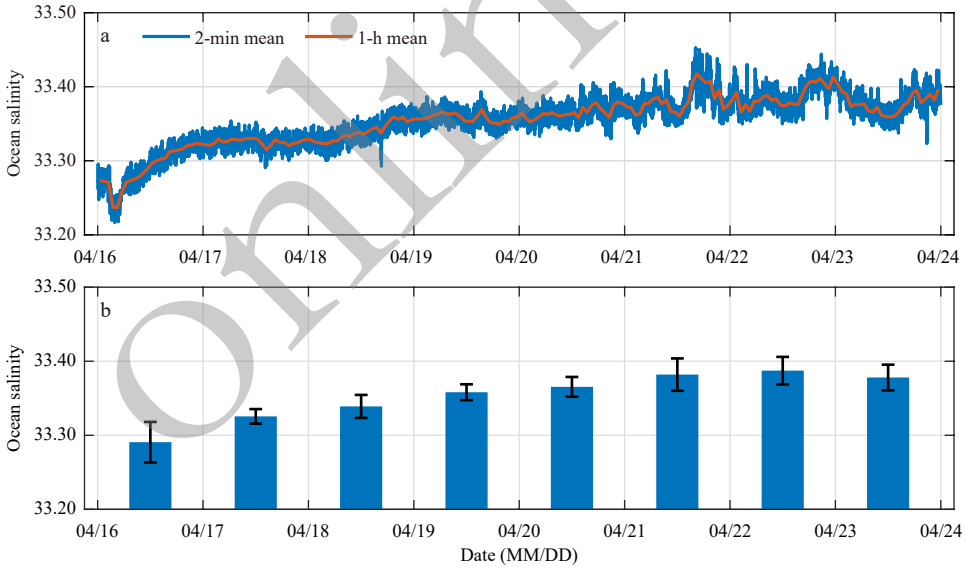

Fig. 3. The ocean salinity observed by CTD at 2 m beneath the landfast ice surface from April 16 to 23 (a) and the daily mean salinity and standard deviation of each day (b).

In the residual method, the vertical gradient of ice temperature is important when calculating the conductive heat flux (F_c). In the cold and snow-free conditions, the vertical temperature profile was approximately linear, while the vertical temperature profile in the thick snow or warm cases was not linear (Lei et al., 2010; Zhao et al., 2019). Therefore, a reference layer (close to the

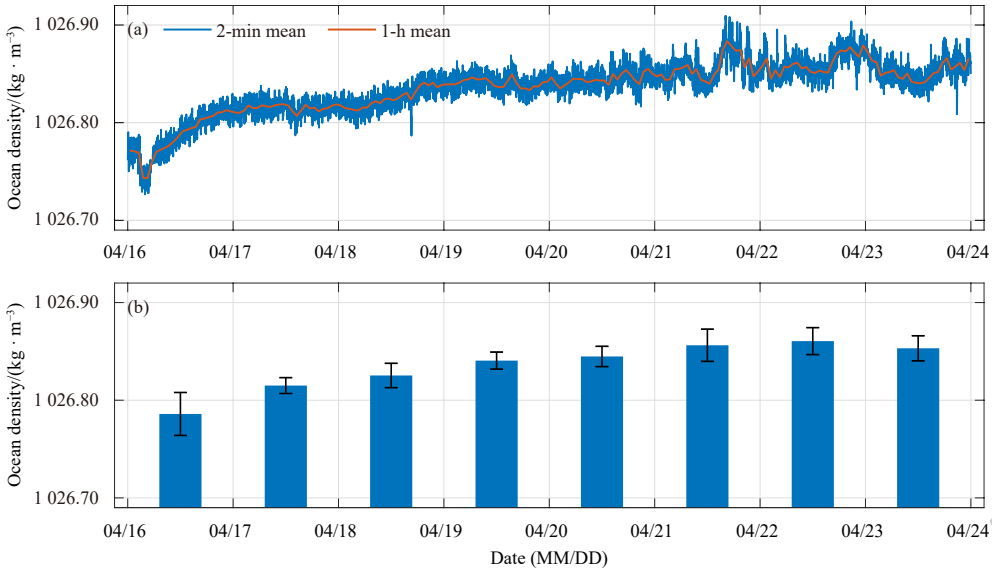

Fig. 4. The ocean density calculated by the temperature and salinity observed by CTD at 2 m beneath the landfast ice surface from April 16 to 23 (a) and the daily mean ocean density and standard deviation of each day (b).

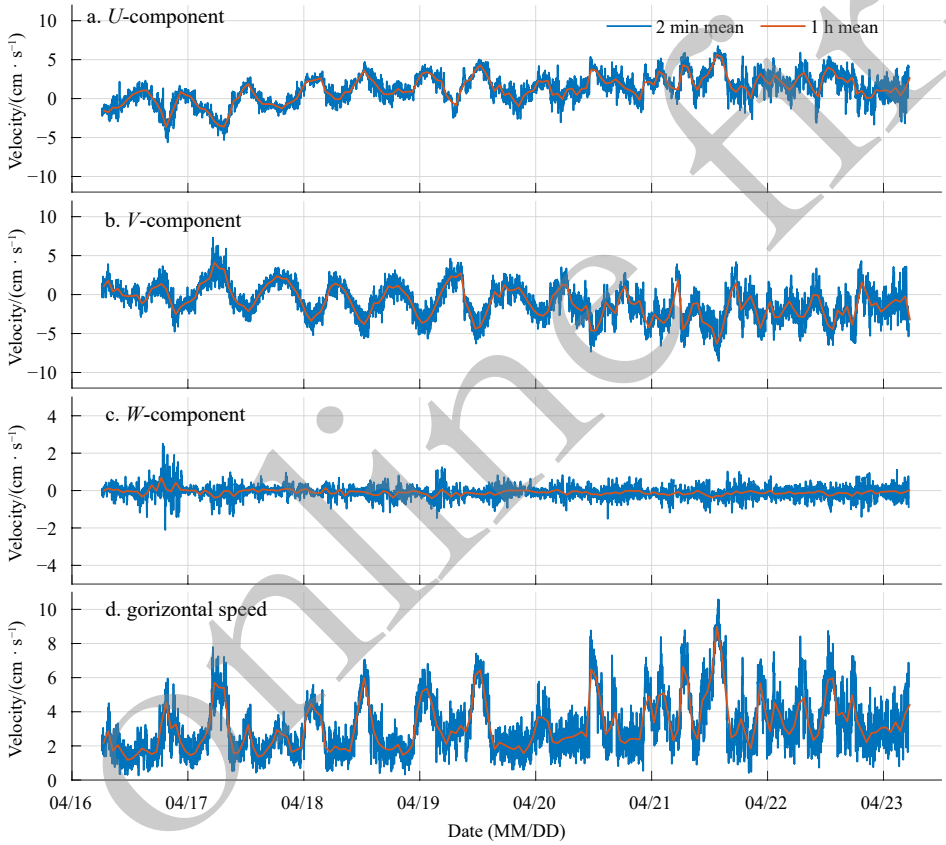

Fig. 5. The time series of ocean current velocity beneath the landfast ice observed by ADV from April 16 to 23. a. *U*-component; b. *V*-component; c. *W*-component; d. horizontal speed.

bottom of the ice) is usually used to calculate the conductive heat flux. McPhee and Untersteiner (1982) chose a reference layer of 0.4 m above the ice bottom. Perovich and Elder (2002) used several reference layers between 0.4–0.8 m above the ice bottom for different ice thickness conditions. Lei et al. (2014) set the reference layer at 0.4–0.7 m above the ice bottom. In this study, the observed ice thickness was around 0.4 m. Therefore, the reference layer (h) was chosen 0.2 m above the ice bottom. The vertical temperature gradient in F_c was calculated using the SIMBA's 2 cm interval temperature profile. The freezing points were estimated by Eq. (5) based on the ocean salinity observations recorded by the CTD. There is a possible difference between ice bottom salinity and 2 m depth salinity, but there are no detailed observations in this region.

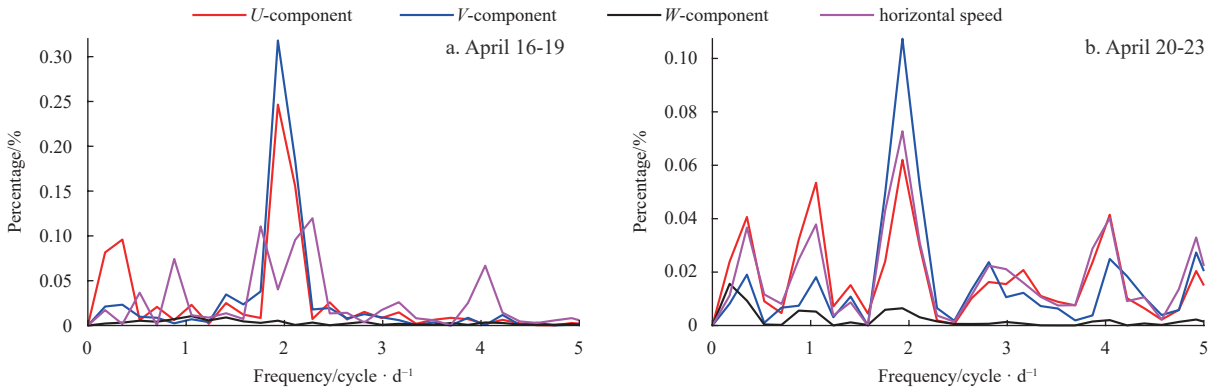

Fig. 6. The spectral analysis of ocean currents during April 16–19 (a) and April 20–23 (b), respectively. The periodogram method was used to detect the periodicity (Welch, 1967).

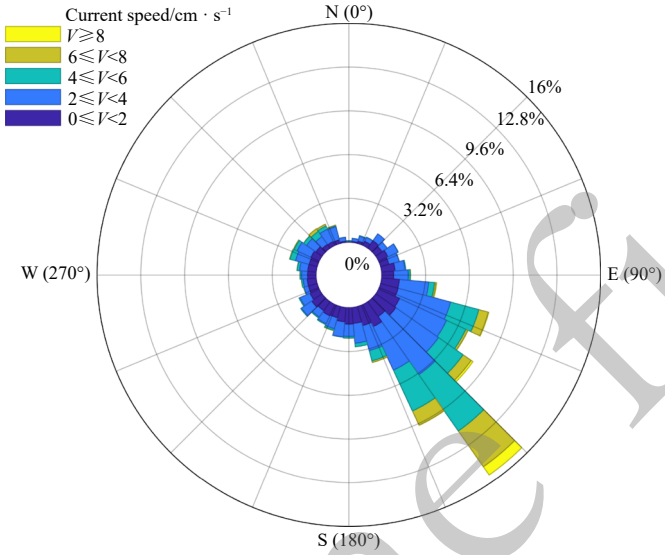

Fig. 7. Roses diagram of the 2-min mean horizontal speed during April 16–23.

Figure 8 shows the heat fluxes in the residual method. The variation of the latent heat flux (F_l) was strongly correlated with the growth and ablation of sea ice. From April 16 to 19, the sea ice bottom was freezing, and F_l was negative. From April 20 to 23, a 2-cm melting occurred at the ice bottom due to sudden ocean warming, and F_l was positive. F_s was relatively smaller throughout the investigation period, varying around 0. The mean oceanic heat flux was (35.1 ± 18.2) W/m² during the whole study period and showed a significant increase and reached the maximum on April 21 (69.4 ± 4.3) W/m²). The mean oceanic heat flux was (24.2 ± 7.6) W/m² during April 16–19 and nearly doubled (44.8 ± 19.4) W/m²) during April 20–23, which led to a 2 cm ice bottom melting.

In contrast to the residual method, bulk parameterisation methods were developed when ocean observations were available (McPhee, 1979, 1992; Sirevaag, 2009; Kirillov et al., 2015).

During April 16–23, the mean freezing point was −1.828℃, gradually decreasing to the minimum of −1.834℃ on April 21, along with increased ocean salinity. The height of ocean temperature above the freezing point (ΔT) increased gradually, from (0.23 ± 0.03)℃ during April 16–19 to (0.36 ± 0.08)℃ during April 20–23.

In the bulk parameterisation method, the mean oceanic heat flux was (32.3 ± 20.2) W/m² during April 16–23, increasing from (21.7 ± 11.1) W/m² during April 16–19 to a nearly double value of (44.8 ± 21.3) W/m² during April 20–23 (Table 1).

The diurnal variations of oceanic heat flux produced from the two methods were similar (Fig. 9b), which were relatively small before April 20 and increased significantly afterwards. Compared with the residual method, the daily variance of the bulk parameterisation method was more significant, which may relate to the high sampling frequency of ocean observations.

The F_w results in this study by residual method (15–75 W/m²) and bulk parameterisation (10–90 W/m²) are similar to those of previous observations, but the peak value of oceanic heat flux is larger. Moreover, the bulk parameterisation method based on high-frequency observational data provides a more detailed characterisation of the variability in oceanic heat flux.

4.2 *The observed melt in the ice bottom*

During the sudden ocean warming event, the ice bottom also changed significantly. SIMBA recorded the vertical temperature profiles through the atmosphere–snow–sea ice–ocean column. As Fig. 10a shows, the mean air temperature during April 16–23 was about (−10.85 ± 3.82)℃, and the daily variation of the mean air temperature was significant, up to 6.46℃ between two adjacent days. The ice temperature showed a significant gradient between 0.11℃/cm and 0.24℃/cm. The ocean temperature

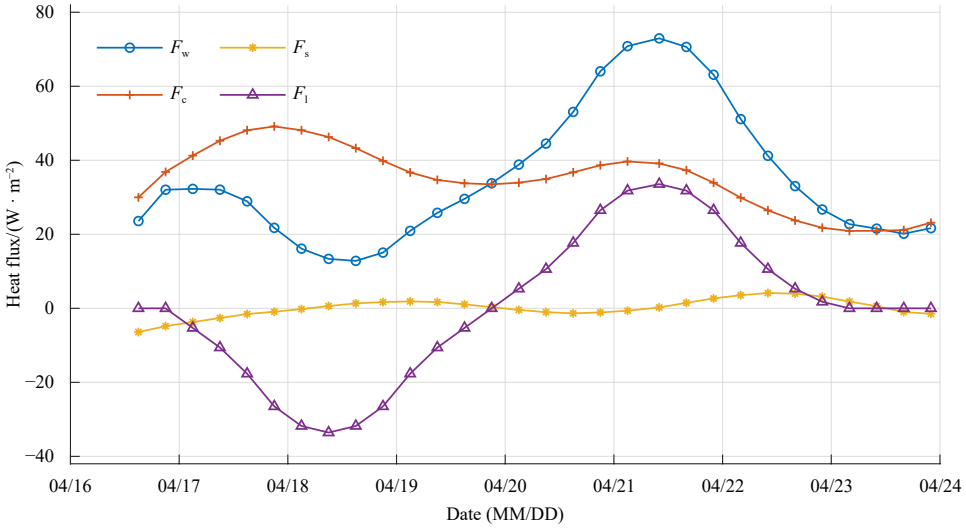

Fig. 8. Conductive heat flux (F_c), latent heat flux (F_l), specific heat flux (F_s) and oceanic heat flux (F_w) were estimated using the residual method. The calculation interval is 6 h.

Table 1. Inter-comparisons of mean oceanic heat flux of two methods

Methods	Mean oceanic heat flux/(W · m^{-2})		
	April 16–19	April 20–23	Totally
Residual method	24.2 ± 7.6	44.8 ± 19.4	35.1 ± 18.2
Bulk parameterization method	21.7 ± 11.1	44.8 ± 21.3	32.3 ± 20.2

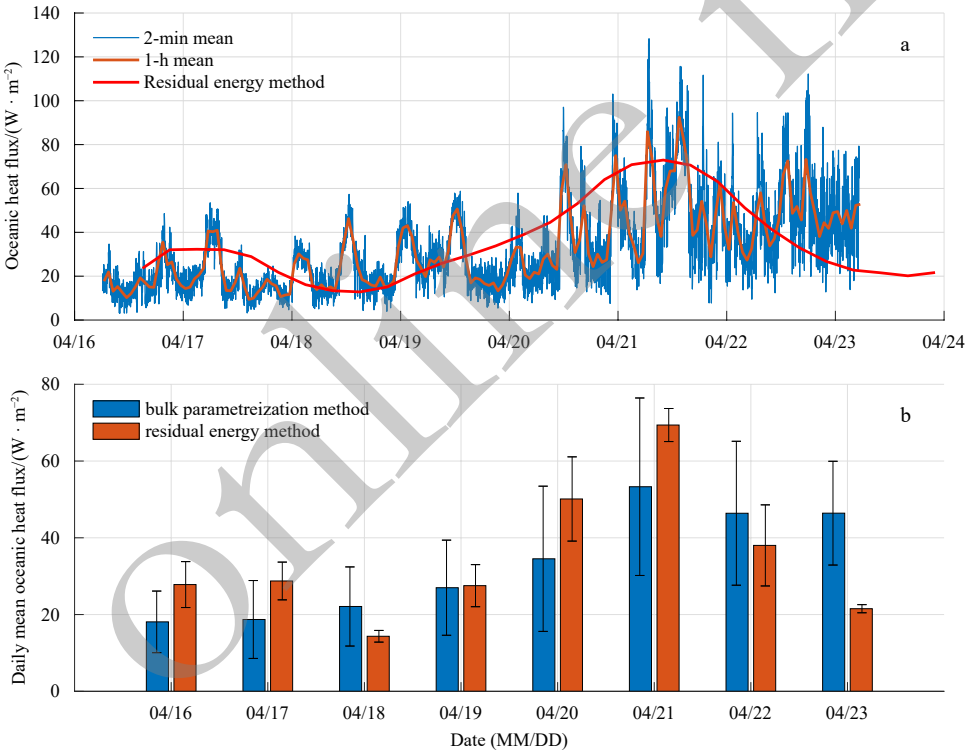

Fig. 9. High-resolution oceanic heat flux calculated by bulk parameterisation method (a) and daily mean oceanic heat flux calculated by two different methods: bulk parameterisation method and residual method (b). In a, the blue and red lines represented 2-min mean and 1-h mean results, respectively, and the bold red lines represented ocean heat fluxes calculated using the residual method. The error bars in b represent ±1 standard deviation.

maintained –1.70℃~–1.90℃, close to the freezing point. The ice thickness was estimated through visual interpretation of the temperature profile of the SIMBA temperature chain according to the method of Zhao et al. (2017b).

The results showed an increase of 2 cm from April 16 to 21, consistent with the increase of ice thickness from 0.44 m to 0.46

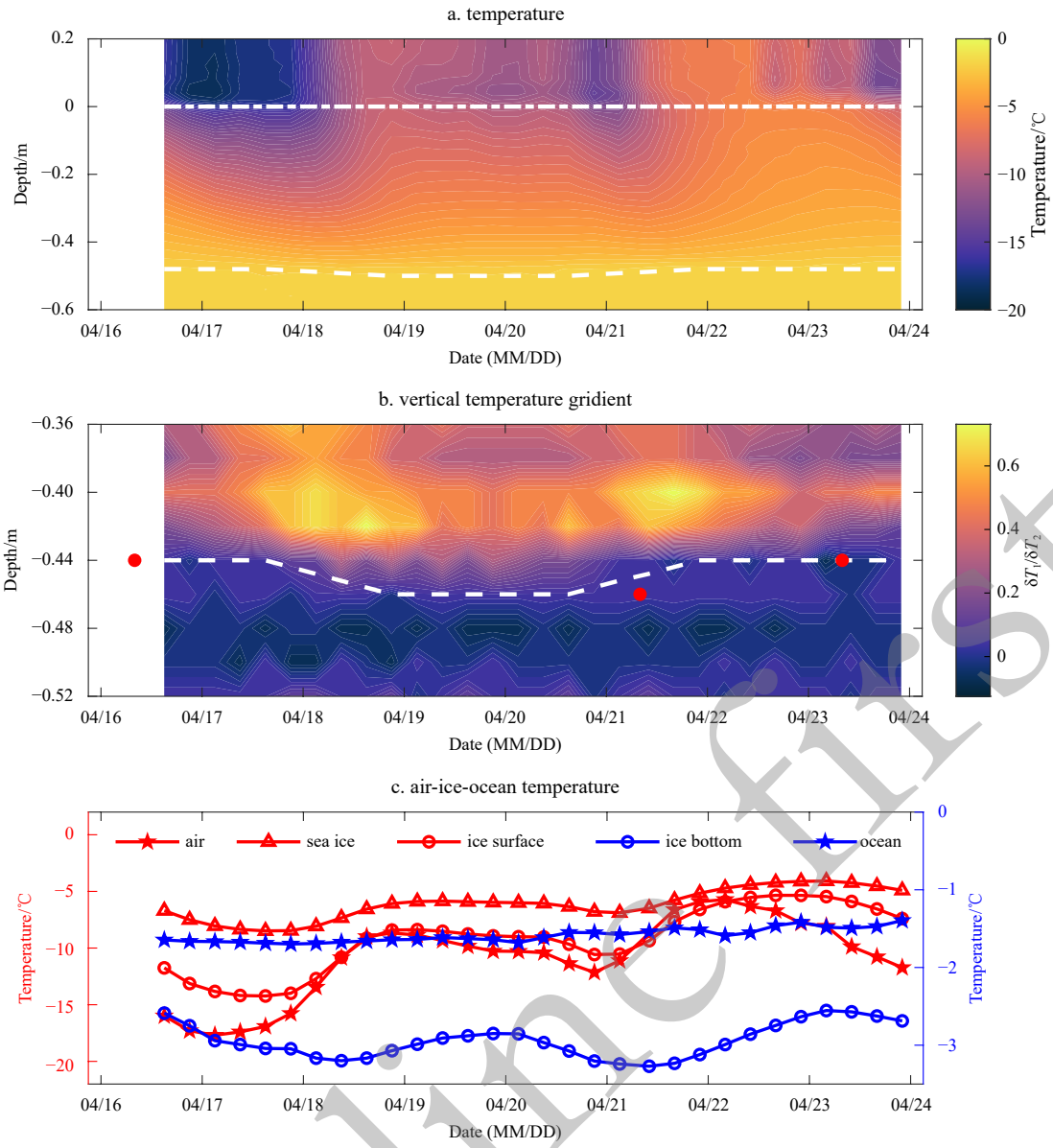

Fig. 10. Vertical temperature profiles (a), vertical temperature gradient (b) and air temperature, mean sea ice temperature, ice surface temperature (the mean of five sensors near the ice surface), ice bottom temperature (the mean of five sensors near the ice bottom), and ocean temperature (the mean of five sensors at the bottom of the temperature chain at a depth of about 3 m from the sea ice surface), recorded by SIMBA (c). The asterisk white solid and white dotted lines in a are the ice bottom and surface, respectively. In b, the white dotted line is the ice bottom, and the red points are the ice bottom position obtained by borehole drilling.

m recorded by the borehole drilling in the field. Soon afterwards, a 2-cm ice bottom melting was detected by SIMBA from April 21 to 23, along with the sudden rise of ocean temperature and corresponding ocean-to-ice heat flux. The borehole drilling also confirmed this ice bottom melt. During the study period, air temperature and ice surface temperature increased gradually. The gradual increase in sea ice temperature reduced the temperature gradient within the sea ice (Fig. 10c). Therefore, warm air also contributed to the 2-cm ice bottom melt during April 20–23.

5 Discussions

5.1 *TPotential influences of the tide on sudden ocean warming*

The current recorded by ADV indicated diurnal back-and-forth ocean movements under the landfast ice cover in the influences of tides, and the results of the further analysis indicated a dominant direction of the southeast (34% of total records). The tidal oscillations were reconstructed using the harmonic analysis method (Pan et al., 2018), and the harmonic constants come from E et al. (2013). The hourly tidal level experienced a decrease from around 1.3 m on April 16 to around 0.5 m on April 23 (Fig. 11), which indicates that the vertical mixing induced by the tides decreased. Meanwhile, the tide period gradually changed from 0.5 d to 1 d after April 21, indicating that the tide pattern changed from semi-diurnal to diurnal.

The comparison of current direction and ocean temperature measured by ADV indicates that the southeast (120–150°) current was the dominant component during the study period (Fig. 12a). Figure 12b shows the ocean temperature and salinity evolution observed by CTD. The ocean mass changed from low temperat-

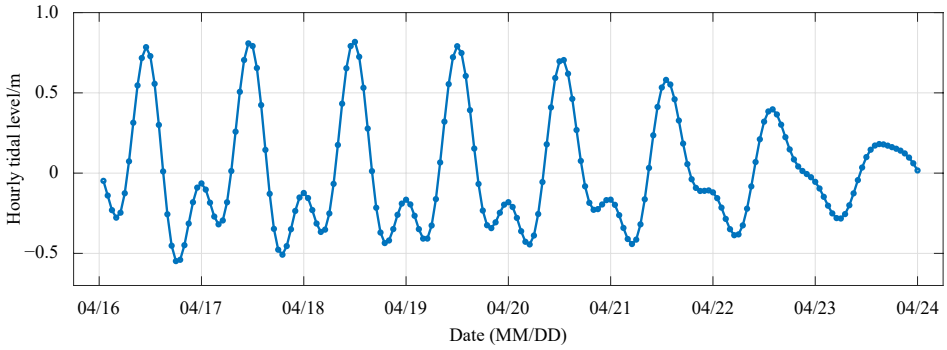

Fig. 11. Hourly tidal levels constructed by the harmonic analysis method.

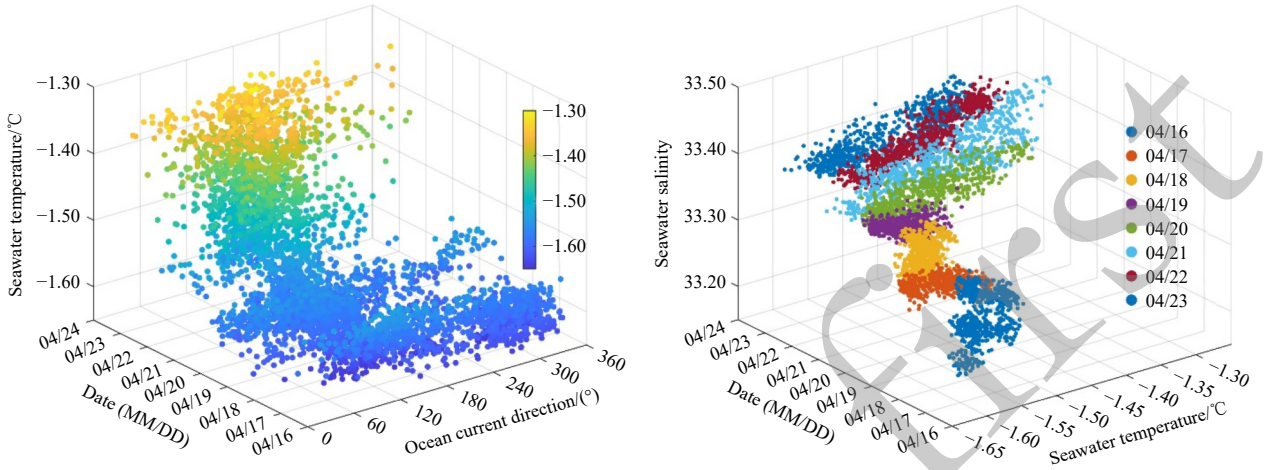

Fig. 12. The 3-D evolution of ocean current direction measured by ADV and ocean temperature measured by CTD (a) and the 3-D time-dependent distribution of ocean temperature and salinity measured by CTD (b).

ure and low salt ((−1.59 ± 0.02)℃ and 33.29 ± 0.03 on April 16) to high temperature and high salt ((−1.45 ± 0.07)℃ and 33.38 ± 0.02 on April 23). These phenomena may be related to the weakening of tide-induced vertical mixing during this period.

5.2 *Potential influence of polar cyclone on air warming*

In this study, the cyclone activities in the Prydz Bay (65°–70°S, 70°–80°E) and the outer Southern Ocean (50°–70°S, 50°–100°E) were statistically analysed. The hourly mean sea level pressure in the hourly ERA5 dataset was averaged to obtain the daily mean sea level pressure from April 16 to 24 (Fig. 13). Meanwhile, the changes in mean sea level pressure, 2-m air temperature and 10-m wind speed in Prydz Bay were calculated (Fig. 14) to analyse the influence of polar cyclone activities on the air temperature and sea ice concentration.

Two cyclones traversed Prydz Bay from west to east during the study period. On April 17, a cyclone structure (cyclone A) formed on the western side of Prydz Bay (Fig. 13b) and gradually progressed eastward along the Antarctic continent when the 2-m air temperature was –18℃ in Prydz Bay and sea ice concentration was 75%. By April 19, cyclone A reached the outer edge of Prydz Bay, exhibiting a minimum central pressure of 960 hPa (Fig. 13c). The intensification of cyclone A brought an influx of warm air, causing a rapid increase in the average 2-m air temperature within Prydz Bay to –11.7℃, with an average maximum wind speed of approximately 14 m/s. As cyclone A continued its eastward progression on April 19, mean sea level pressure within Prydz Bay partially recovered to 973 hPa, wind speeds weakened, and temperatures slightly decreased. Concurrently, a new cyclone (Fig. 13d, cyclone B) formed on the western side of Prydz Bay, exhibiting a lower central pressure (948 hPa) and longer duration than cyclone A. During April 20–21, the mean air temperature was –10.4℃, and the mean wind speed was 11 m/s. The successive passage of two cyclones increased sea ice concentration to 90% in Prydz Bay (Fig. 10c). Therefore, the cyclones caused a significant rise in air temperature (about 10℃ increment) and the concentration of sea ice (from 75% to 90%), which were both favours of the sudden warm of ocean temperature.

5.3 *Sensitivity experiments of oceanic heat flux*

Sensitivity experiments were conducted to estimate the response of ice growth rate to the different oceanic heat flux. Ice growth rate was firstly calculated based on Eq. (1), with oceanic heat flux from the bulk method as shown in Fig. 9a. This can be considered as the control run and named as Exp. A. Two sets of sensitivity experiments were defined: Exp. B assuming no sudden ocean warming and maintained the mean ocean temperature (–1.60℃) during April 16–19 to the subsequent period of April 20–23; Exp. C assuming no oceanic heat flux in the subsequent period of April 20–23.

In Exp. A, ice growth rate during April 16–19 was 0.6 cm/d, leading to an ice thickness increase of 2.3 cm; while during April 20–23, ice growth rate was –0.5 cm/d, and ice thickness decreased by 1.9 cm. The calculated increase and decrease were in line with the measurement results. Exp. B assumed that no ocean temperature rise occurred after April 20. Ocean temperature re-

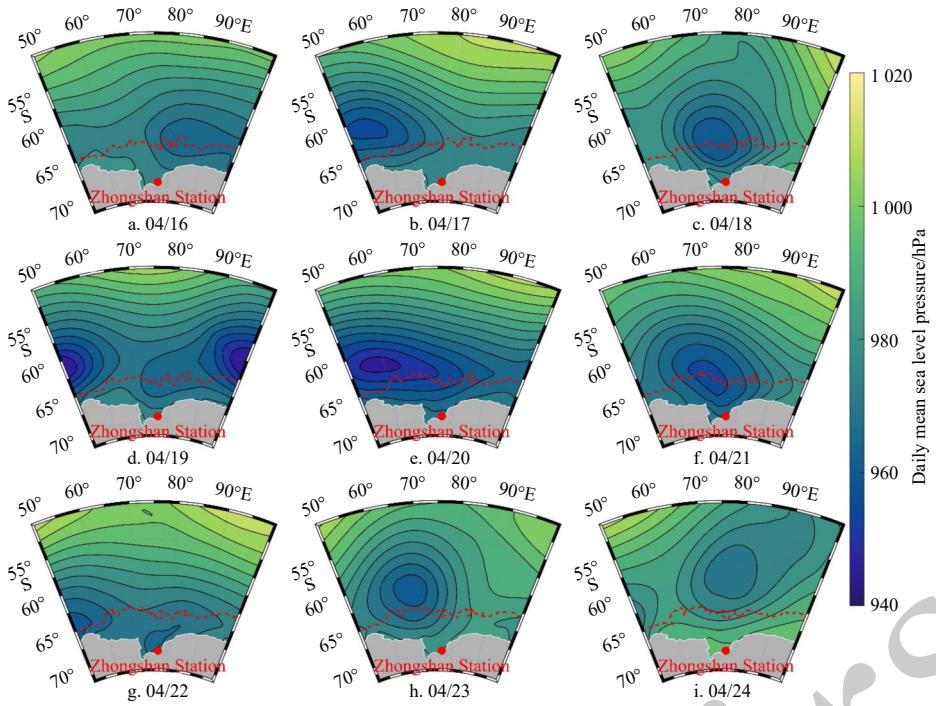

Fig. 13. Evolution of the daily mean sea level pressure in the Southern Ocean off Prize Bay (50°–70°S, 50°–100°E) from April 16 to 24, 2021. The reanalysis product was retrieved from the ERA5 hourly data, provided by ECMWF (https://cds.climate.copernicus.eu), with a spatial resolution of 0.25° × 0.25°. The red dotted line is the sea ice edge (SIC = 15%).

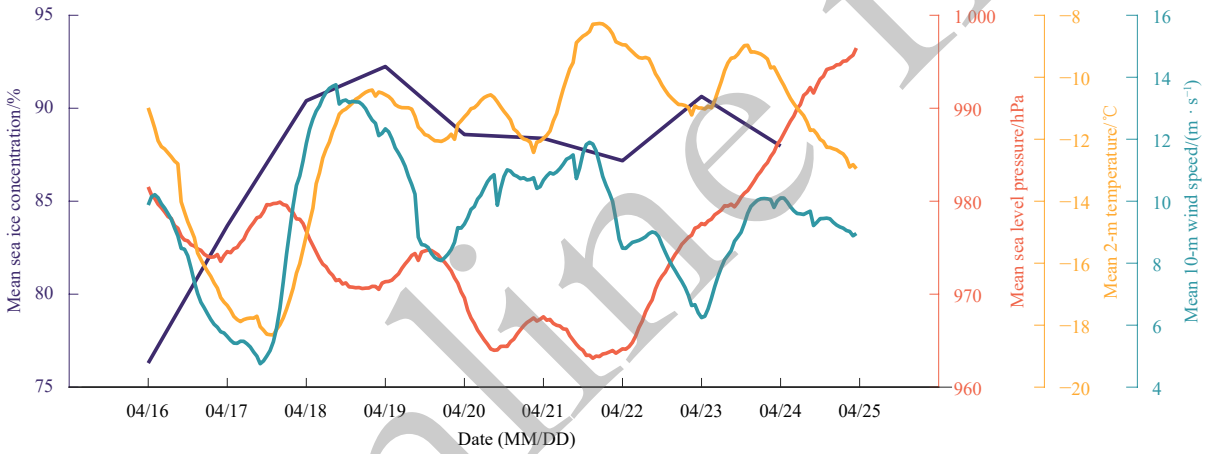

Fig. 14. During the study period, the atmospheric and sea ice concentration in Prize Bay (65°–70°S, 70°–80°E). The purple line represents the average sea ice concentration in Prydz Bay; the red line represents the mean sea level pressure; the yellow line represents the mean 2-m temperature; and the green line represents the mean 10-m wind speed.

mained constant at –1.60℃ (mean during April 16–19) to subsequent period of April 20–23, and the corresponding mean oceanic heat flux was (29.0 ± 12.5) W/m^2, 35% smaller than the actual conditions. The ice growth rate during April 20–23 was 0.1 cm/d, and ice thickness would increase 0.3 cm. If oceanic heat flux was ignored in Exp. C, landfast ice showed a larger rate of 1.3 cm/d, and the ice thickness would increase by 9.6 cm.

6 Conclusions

The ice-ocean boundary layer beneath sea ice cover plays a vital role in the growth and melting of sea ice. An integrated high-frequency ice-ocean observation system, including Acoustic Doppler Velocimeter, Conductivity Temperature and Depth Sensor, and Sea Ice Mass Balance Array, was deployed in the landfast ice region close to the Chinese Zhongshan Station in Antarctica. The observed minute-resolution ocean temperature, salinity, density, current, and heat flux were analysed and a sudden ocean warming event occurred during 16–23 April and was further investigated in this study.

The sudden ocean warming shifted the growth phase to melt phase at the ice bottom. The CTD at 5 m beneath the landfast ice surface recorded a jump increase of ocean temperature ($p < 0.01$) from (–1.60 ± 0.03)℃ during April 16–19 to (–1.46 ± 0.07)℃ during April 20–23. Meanwhile, the SIMBA temperature chain recorded that landfast ice froze by 2 cm at the bottom during April 16–20 while melting by 2 cm during April 21–23.

The salt rejection at the ice bottom slow down and the growth rate of ocean salinity and density decreased. The mean ocean sa-

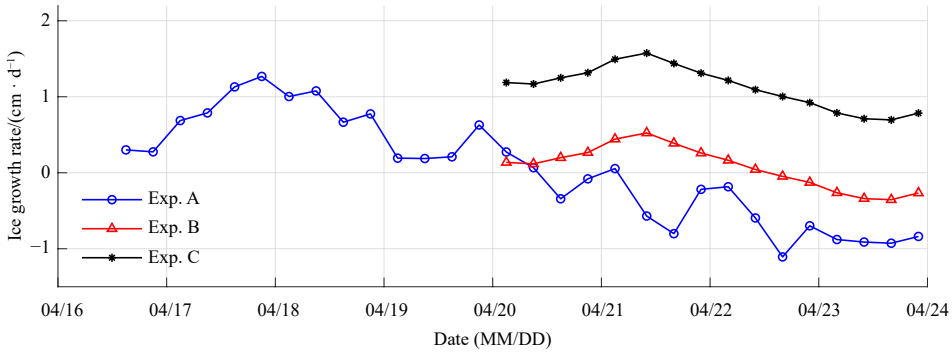

Fig. 15. The ice growth rate from different experiments of oceanic heat fluxes. The time interval of the calculations is 6 h.

linity and density were 33.53 ± 0.03 and (1 026.84 ± 0.02) kg/m³ during the study period. The ocean current recorded by ADV showed that 34% of the current direction was southeast (120°–150°), and the mean velocity was (3.1 ± 1.7) cm/s, with a maximum up to 10.6 cm/s for 2 min time series and 9.0 cm/s for hourly mean time series.

The sudden ocean warming lead to increasing of oceanic heat fluxes. The estimated values became double after April 20, which was related to both the increase in ocean current velocity (from 2.69 cm/s to 3.68 cm/s) and the rise of ocean temperature (from −1.60℃ to −1.46℃). The increase in oceanic heat flux was the direct trigger on 2 cm basal melt of the landfast ice thickness.

The tide transformation from semi-diurnal to diurnal during the study period was possibly attributed to the significant rise in ocean temperature. From April 16–23, the tidal amplitude weakened, and the period of current variation became longer. Two cyclones passed across Prydz Bay during the study period, which brought warm air and increased the air temperature, as the observations show. The sensitivity experiments with different oceanic heat fluxes showed that in the absence of sudden ocean warming events, the ice bottom would grow by about 0.3 cm from April 20–23. Therefore, the ocean currents influenced by the coastal tide and the local atmosphere conditions played essential roles in the ocean temperature and further affected the oceanic heat flux and the ice growth.

In this study, the high frequency of oceanic measurements provides a chance to investigate the influences of oceanic regimes beneath landfast ice on the diurnal scale. The current analysis timeframe is limited. Additional years of field observations will be undertaken to acquire an extended time series of data and to delve deeper into the intricacies of air–ice–ocean interactions.

Acknowledgement

We are grateful to Antarctic Zhongshan Ice and Space Environment National Observation and Research Station of Polar Research Institute of China for providing the experimental sites and relevant supports.

References

Allison I. 1981. Antarctic ice growth and oceanic heat flux. IAHS Publication, (131): 161–170

Bigg P H. 1967. Density of water in SI units over the range 0–40 C. British Journal of Applied Physics, 18(4): 521–525, doi: 10.1088/0508-3443/18/4/315

E Dongchen, Huang Jifeng, Zhang Shengkai. 2013. Analysis of tidal features of Zhongshan Station, East Antarctic. Geomatics and Information Science of Wuhan University (in Chinese), 38(4): 379–382,464

Ebert E E, Schramm J L, Curry J A. 1995. Disposition of solar radiation in sea ice and the upper ocean. Journal of Geophysical Research: Oceans, 100(C8): 15965–15975, doi: 10.1029/95JC01672

Guo Guijun, Shi Jiuxin, Gao Libao, et al. 2019. Reduced sea ice production due to upwelled oceanic heat flux in Prydz Bay, East Antarctica. Geophysical Research Letters, 46(9): 4782–4789, doi: 10.1029/2018GL081463

Guo Guijun, Shi Jiuxin, Jiao Yutian. 2015. Temporal variability of vertical heat flux in the Makarov Basin during the ice camp observation in summer 2010. Acta Oceanologica Sinica, 34(11): 118–125, doi: 10.1007/s13131-015-0755-z

Heil P. 2006. Atmospheric conditions and fast ice at Davis, East Antarctica: A case study. Journal of Geophysical Research: Oceans, 111(C5): C05009

Heil P, Allison I, Lytle V I. 1996. Seasonal and interannual variations of the oceanic heat flux under a landfast Antarctic sea ice cover. Journal of Geophysical Research: Oceans, 101(C11): 25741–25752, doi: 10.1029/96JC01921

Hersbach H, Bell B, Berrisford P, et al. 2020. The ERA5 global reanalysis. Quarterly Journal of the Royal Meteorological Society, 146(730): 1999–2049, doi: 10.1002/qj.3803

Himmich K, Vancoppenolle M, Madec G, et al. 2023. Drivers of Antarctic sea ice advance. Nature Communications, 14: 6219, doi: 10.1038/s41467-023-41962-8

Hu Haihan, Zhao Jiechen, Heil P, et al. 2023. Annual evolution of the ice–ocean interaction beneath landfast ice in Prydz Bay, East Antarctica. The Cryosphere, 17(6): 2231–2244, doi: 10.5194/tc-17-2231-2023

Huang N E, Shen Z, Long S R, et al. 1998. The empirical mode decomposition and the Hilbert spectrum for nonlinear and non-stationary time series analysis. Proceedings of the Royal Society of London. Series A: Mathematical, Physical and Engineering Sciences, 454(1971): 903–995

Kirillov S, Dmitrenko I, Babb D, et al. 2015. The effect of ocean heat flux on seasonal ice growth in Young Sound (Northeast Greenland). Journal of Geophysical Research: Oceans, 120(7): 4803–4824, doi: 10.1002/2015JC010720

Lei Ruibo, Cheng Bin, Hoppmann M, et al. 2022. Seasonality and timing of sea ice mass balance and heat fluxes in the Arctic transpolar drift during 2019–2020. Elementa: Science of the Anthropocene, 10(1): 000089, doi: 10.1525/elementa.2021.000089

Lei Ruibo, Li Zhijun, Cheng Bin, et al. 2010. Annual cycle of landfast sea ice in Prydz Bay, east Antarctica. Journal of Geophysical Research: Oceans, 115(C2): C02006

Lei Ruibo, Li Na, Heil P, et al. 2014. Multiyear sea ice thermal regimes and oceanic heat flux derived from an ice mass balance buoy in the Arctic Ocean. Journal of Geophysical Research: Oceans, 119(1): 537–547, doi: 10.1002/2012JC008731

Li Na, Lei Ruibo, Heil P, et al. 2023. Seasonal and interannual variability of the landfast ice mass balance between 2009 and 2018 in Prydz Bay, East Antarctica. The Cryosphere, 17(2): 917–937, doi: 10.5194/tc-17-917-2023

Li Xinqing, Shokr M, Hui Fengming, et al. 2020. The spatio-temporal patterns of landfast ice in Antarctica during 2006–2011 and 2016–2017 using high-resolution SAR imagery. Remote Sensing of Environment, 242: 111736, doi: 10.1016/j.rse.2020.111736

Lytle V I, Massom R, Bindoff N, et al. 2000. Wintertime heat flux to the underside of East Antarctic pack ice. Journal of Geophysical Research: Oceans, 105(C12): 28759–28769, doi: 10.1029/2000JC900099

Massom R A, Giles A B, Fricker H A, et al. 2010. Examining the interaction between multi-year landfast sea ice and the Mertz Glacier Tongue, East Antarctica: Another factor in ice sheet stability?. Journal of Geophysical Research: Oceans, 115(C12): C12027

Massom R, Hill K, Barbraud C, et al. 2009. Fast ice distribution in Adélie Land, East Antarctica: interannual variability and implications for emperor penguins *Aptenodytes forsteri*. Marine Ecology Progress Series, 374: 243–257, doi: 10.3354/meps07734

Maykut G A. 1986. The surface heat and mass balance. In: Untersteiner N, ed. The Geophysics of Sea Ice. New York: Springer, 395–463

Maykut G A, McPhee M G. 1995. Solar heating of the Arctic mixed layer. Journal of Geophysical Research: Oceans, 100(C12): 24691–24703, doi: 10.1029/95JC02554

Maykut G A, Untersteiner N. 1971. Some results from a time-dependent thermodynamic model of sea ice. Journal of Geophysical Research, 76(6): 1550–1575., doi: 10.1029/JC076i006p01550

McMinn A, Ashworth C, Ryan K. 2000. In situ net primary productivity of an Antarctic fast ice bottom algal community. Aquatic Microbial Ecology, 21: 177–185, doi: 10.3354/ame021177

McPhee M G. 1979. The effect of the oceanic boundary layer on the mean drift of pack ice: Application of a simple model. Journal of Physical Oceanography, 9(2): 388–400, doi: 10.1175/1520-0485(1979)009<0388:TEOTOB>2.0.CO;2

McPhee M G. 1992. Turbulent heat flux in the upper ocean under sea ice. Journal of Geophysical Research: Oceans, 97(C4): 5365–5379, doi: 10.1029/92JC00239

McPhee M G. 2002. Turbulent stress at the ice/ocean interface and bottom surface hydraulic roughness during the SHEBA drift. Journal of Geophysical Research: Oceans, 107(C10): 8037

McPhee M G, Ackley S F, Guest P, et al. 1996. The Antarctic zone flux experiment. Bulletin of the American Meteorological Society, 77(6): 1221–1232, doi: 10.1175/1520-0477(1996)077<1221:TAZFE>2.0.CO;2

McPhee M G, Kottmeier C, Morison J H. 1999. Ocean heat flux in the central Weddell Sea during winter. Journal of Physical Oceanography, 29(6): 1166–1179, doi: 10.1175/1520-0485(1999)029<1166:OHFITC>2.0.CO;2

McPhee M G, Morison J H, Nilsen F. 2008. Revisiting heat and salt exchange at the ice-ocean interface: Ocean flux and modeling considerations. Journal of Geophysical Research: Oceans, 113(C6): C06014

McPhee M G, Untersteiner N. 1982. Using sea ice to measure vertical heat flux in the ocean. Journal of Geophysical Research: Oceans, 87(C3): 2071–2074, doi: 10.1029/JC087iC03p02071

Meehl G A, Arblaster J M, Chung C T Y, et al. 2019. Sustained ocean changes contributed to sudden Antarctic sea ice retreat in late 2016. Nature Communications, 10: 14, doi: 10.1038/s41467-018-07865-9

Miles B W J, Stokes C R, Jamieson S S R. 2017. Simultaneous disintegration of outlet glaciers in Porpoise Bay (Wilkes Land), East Antarctica, driven by sea ice break-up. The Cryosphere, 11(1): 427–442, doi: 10.5194/tc-11-427-2017

Millero F J. 1978. Freezing point of seawater. Eighth Report of the Joint Panel on Oceanographic Tables and Standards (JPOTS). UNESCO technical papers in marine sciences. 28: 29–35

Millero F J, Poisson A. 1981. International one-atmosphere equation of state of seawater. Deep-Sea Research Part A. Oceanographic Research Papers, 28(6): 625–629

Moreau S, Boyd P W, Strutton P G. 2020. Remote assessment of the fate of phytoplankton in the Southern Ocean sea-ice zone. Nature Communications, 11: 3108, doi: 10.1038/s41467-020-16931-0

Pan Haidong, Lv Xianqing, Wang Yingying, et al. 2018. Exploration of tidal-fluvial interaction in the Columbia River Estuary using S_TIDE. Journal of Geophysical Research: Oceans, 123(9): 6598–6619, doi: 10.1029/2018JC014146

Parkinson C L, Cavalieri D J. 2012. Antarctic sea ice variability and trends, 1979–2010. The Cryosphere, 6(4): 871–880, doi: 10.5194/tc-6-871-2012

Perovich D K, Elder B. 2002. Estimates of ocean heat flux at SHEBA. Geophysical Research Letters, 29(9): 58-1–58-4.

Peterson A K, Fer I, McPhee M G, et al. 2017. Turbulent heat and momentum fluxes in the upper ocean under Arctic sea ice. Journal of Geophysical Research: Oceans, 122(2): 1439–1456, doi: 10.1002/2016JC012283

Purdie C R, Langhorne P J, Leonard G H, et al. 2006. Growth of first-year landfast Antarctic sea ice determined from winter temperature measurements. Annals of Glaciology, 44: 170–176, doi: 10.3189/172756406781811853

Purich A, Doddridge E W. 2023. Record low Antarctic sea ice coverage indicates a new sea ice state. Communications Earth & Environment, 4: 314

Semtner A J. 1976. A model for the thermodynamic growth of sea ice in numerical investigations of climate. Journal of Physical Oceanography, 6(3): 379–389, doi: 10.1175/1520-0485(1976)006<0379:AMFTTG>2.0.CO;2

Singh H K A, Landrum L, Holland M M, et al. 2021. An overview of Antarctic sea ice in the community earth system model version 2, Part I: Analysis of the seasonal cycle in the context of sea ice thermodynamics and coupled atmosphere-ocean-ice processes. Journal of Advances in Modeling Earth Systems, 13(3): e2020MS002143, doi: 10.1029/2020MS002143

Sirevaag A. 2009. Turbulent exchange coefficients for the ice/ocean interface in case of rapid melting. Geophysical Research Letters, 36(4): L04606

Sirevaag A, Fer I. 2009. Early spring oceanic heat fluxes and mixing observed from drift stations north of Svalbard. Journal of Physical Oceanography, 39(12): 3049–3069, doi: 10.1175/2009JPO4172.1

Stammerjohn S, Massom R, Rind D, et al. 2012. Regions of rapid sea ice change: An inter-hemispheric seasonal comparison. Geophysical Research Letters, 39(6): L06501

Untersteiner N. 1961. On the mass and heat budget of arctic sea ice. Archiv für Meteorologie, Geophysik und Bioklimatologie Serie A, 12(2): 151–182

Welch P. 1967. The use of fast Fourier transform for the estimation of power spectra: A method based on time averaging over short, modified periodograms. IEEE Transactions on Audio and Electroacoustics, 15(2): 70–73, doi: 10.1109/TAU.1967.1161901

Yang Yu, Li Zhijun, Leppäranta M, et al. 2016. Modelling the thickness of landfast sea ice in Prydz Bay, East Antarctica. Antarctic Science, 28(1): 59–70, doi: 10.1017/S0954102015000449

Zhang Liping, Delworth T L, Yang Xiaosong, et al. 2022. The relative role of the subsurface Southern Ocean in driving negative Antarctic Sea ice extent anomalies in 2016–2021. Communications Earth & Environment, 3: 302

Zhao Jiechen, Cheng Jingjing, Tian Zhongxiang, et al. 2022. Snow and ice thicknesses derived from Fast Ice Prediction System Version 2.0 (FIPS V2.0) in Prydz Bay, East Antarctica: comparison with in-situ observations. Big Earth Data, 6(4): 492–503, doi: 10.1080/20964471.2021.1981196

Zhao Jiechen, Cheng Bin, Vihma T, et al. 2020. Fast Ice Prediction System (FIPS) for land-fast sea ice at Prydz Bay, East Antarctica: an operational service for CHINARE. Annals of Glaciology, 61(83): 271–283, doi: 10.1017/aog.2020.46

Zhao Jiechen, Cheng Bin, Yang Qinghua, et al. 2017a. Observations and modelling of first-year ice growth and simultaneous second-year ice ablation in the Prydz Bay, East Antarctica. Annals of Glaciology, 58(75pt1): 59–67, doi: 10.1017/aog.2017.33

Zhao Jiechen, Yang Qinghua, Cheng Bin, et al. 2017b. Snow and land-fast sea ice thickness derived from thermistor chain buoy in the Prydz Bay, Antarctic. Haiyang Xuebao (in Chinese), 39(11): 115–127

Zhao Jiechen, Yang Qinghua, Cheng Bin, et al. 2019. Spatial and temporal evolution of landfast ice near Zhongshan Station, East Antarctica, over an annual cycle in 2011/2012. Acta Oceanologica Sinica, 38(5): 51–61, doi: 10.1007/s13131-018-1339-5